Water vapor radiative effects on short-wave radiation in Spain

Javier Vaquero-Martínez[1], Manuel Antón

Departamento de Física, Universidad de Extremadura, Badajoz (Spain)

Instituto Universitario de Investigación del Agua, Cambio Climático y Sostenibilidad (IACYS), Universidad de Extremadura, Badajoz (Spain)

José Pablo Ortiz de Galisteo

Agencia Estatal de Meteorologia (AEMET), Valladolid (Spain)

Grupo de Óptica Atmosférica, Universidad de Valladolid, Valladolid (Spain)

Roberto Román

Department of Applied Physics, University of Granada, Granada (Spain)

Andalusian Institute for Earth System Research (IISTA-CEAMA), Granada (Spain)

Victoria E. Cachorro

Grupo de Óptica Atmosférica, Universidad de Valladolid, Valladolid (Spain)

Abstract

In this work, water vapor radiative effect (WVRE) is studied by means of the Santa Barbara's Disort Radiative Transfer (SBDART) model, fed with integrated water vapor (IWV) data from 20 ground-based GPS stations in Spain. Only IWV data recorded during cloud-free days (selected using daily insolation data) were used in this study. Typically, for SZA $= 60.0 \pm 0.5°$ WVRE values are around -82 and -66 Wm^{-2} (first and third quartile), although it can reach up -100 Wm^{-2} or decrease to -39 Wm^{-2}. A power dependence of WVRE on IWV and cosine of solar zenith angle (SZA) was found by an empirical fit. This relation is used to determine the water vapor radiative efficiency (WVEFF $= \partial$WVRE$/\partial$IWV). Obtained WVEFF values range from -9 and 0 Wm^{-2}mm^{-1} (-2.2 and 0 %mm^{-1} in relative terms). It is observed that WVEFF decreases

[1]javier_vm@unex.es

as IWV increases, but also as SZA increases. On the other hand, when relative WVEFF is calculated from normalized WVRE, an increase of SZA results in an increase of relative WVEFF. Heating rates were also calculated, ranging from 0.2 $Kday^{-1}$ to 1.7 $Kday^{-1}$. WVRE was also calculated at top of atmosphere, where values ranged from 4 Wm^{-2} to 37 Wm^{-2}.

Keywords: short-wave, radiative effect, radiative efficiency, water vapor, IWV, Iberian Peninsula.

---

1. Introduction

The climate system is interactive, and all its elements (atmosphere, Earth's surface and biosphere) are interconnected (Denman & Brasseur, 2007). Water, presented in its three states in the Earth-atmosphere system, is one of the elements of paramount importance. Water vapor is acknowledged as the most important atmospheric greenhouse gas, and although it is not directly involved in climate change since its concentration is regulated by temperature more than anthropogenic emissions, it causes a positive radiative feedback on climate system (Colman, 2003).

Currently, the radiative effect of water vapor is considered a feedback rather than a forcing, since the water vapor concentration is mainly dependent on the temperature on a global scale, and the typical residence time of water vapor is ten days Myhre et al. (2013). For these reasons, anthropogenic emissions of water vapor have a negligible impact on global climate. The main anthropogenic impact in water vapor content is due to the emission of other greenhouse gases, which cause temperature increase and therefore an increase in water vapor content (Santer et al., 2007). Emissions in the stratosphere, however, can be considered as a forcing (Smith et al., 2001; Forster & Shine, 2002; Zhong & Haigh, 2003; Solomon et al., 2010), because in the stratosphere water vapor emissions (i.e., caused by stratospheric flights) manage to stay in the long term.

Water vapor in the atmosphere can be quantified using the column integrated amount of water vapor (IWV), which is equivalent to condensing all the water

vapor in the atmospheric column and measuring the height that it would reach in a vessel of unit cross section. It can be measured in columnar mass density (gcm^{-2} or kgm^{-2}) or in length (height) units (mm) (Román et al., 2015). The instantaneous water vapor radiative effect (WVRE) at surface is defined as the net change in short-wave (SW) solar radiation at surface taking as reference a dry atmosphere (adapted from Mateos et al., 2013a). It can be also calculated at top of atmosphere (TOA) ($WVRE_{TOP}$). Therefore, water vapor efficiency (WVEFF) can be defined as the variation on WVRE that is caused by an increase of 1 unit of atmospheric water vapor, that is to say, the first derivative of WVRE with respect to IWV.

In this work, the WVEFF focused on the SW range is analyzed using a radiative transfer code fed with IWV data recorded from several GPS ground-based stations in the Iberian Peninsula. Although other works have studied the change in surface radiation due to water vapor (Soden et al., 2002; Di Biagio et al., 2012; Román et al., 2014), none quantifies nor analyzes the WVEFF or WVRE and its dependences on IWV and SZA, as it has already been done for clouds (Mateos et al., 2013b, 2014b), aerosols (Mateos et al., 2013a, 2014a) and ozone (Antón & Mateos, 2013; Antón et al., 2016). This paper aims to be useful for a better understanding of the individual contributions of water vapor to the radiation budget in the Iberian Peninsula, and evaluate the WVEFF under different conditions of SZA and IWV in this context. Knowledge about surface energy balance sensitivity to variations of IWV is important to assess the system's response to future climate changes.

2. Integrated Water Vapor data

IWV data used in this work were recorded from 20 GPS Spanish stations located mostly in the Iberian Peninsula (see Figure 1 and Table 1). For a full description of the method to derive IWV data from GPS, refer to Bevis et al. (1992). In the process of positioning a GPS ground-based station, the fundamental idea is to determine the distance to several GPS satellites in order to triangulate the receiver position. The distance is obtained by measuring the time that the microwave signals take from GPS satellites to GPS receivers. The signals, however, suffer some delays along their way. One of those delays is called the slant tropospheric delay (STD), which is caused by the tropospheric gases. STD is due to two contributions, one related to water molecule's dipolar momentum, slant wet delay (SWD), and a non-dipolar contribution, due to all gases (including water vapor), which is known as slant hydrostatic delay (SHD)

$$\mathrm{STD} = \mathrm{SWD} + \mathrm{SHD} \tag{1}$$

Such delay can be converted to zenith tropospheric delay (ZTD) by applying mapping functions. Mapping functions are different for SHD and SWD, but they are similar, so an approximation can be made

$$\mathrm{STD} = m_{\mathrm{wet}}(E)\mathrm{ZWD} + m_{\mathrm{hydrostatic}}(E)\mathrm{ZHD} = m(E)\mathrm{ZTD} \tag{2}$$

$$\mathrm{ZTD} = \mathrm{ZHD} + \mathrm{ZWD} \tag{3}$$

If pressure at surface is known, ZHD can be modeled, and ZWD obtained from subtracting ZTD minus ZHD. ZWD is proportional to IWV

$$\mathrm{ZWD} = \kappa \mathrm{IWV} \tag{4}$$

The constant κ can be determined from the mean temperature of the atmosphere weighted by the water vapor content. This mean temperature can be estimated from an empirical relationship if temperature at the station level is known.

The dataset used in this work covers from 2007 to 2015. Spanish Geographic Institute "Instituto Geográfico Nacional", which is a local analysis center for the European Reference Frame (EUREF), provided the tropospheric products. Surface pressure and temperature, needed to retrieve IWV from ZTD products, were provided by the Spanish Meteorological State Agency (AEMet). The temperature was interpolated to the time of measurements linearly, and pressure was interpolated as well, taking into account the barometric tide. The IWV dataset obtained has already been used in other works to perform validation exercises on satellite IWV data such as Román et al. (2015); Bennouna et al. (2013); Vaquero-Martínez et al. (2017a,b).

Daily insolation data were provided from AEMet as well. Insolation is divided by the theoretical insolation in a cloud-free situation to obtain an insolation factor. In order to filter out cloudy cases or cases with a significant load of aerosol days with an insolation factor below 0.75 (75%) were not considered. World Meteorological Organization (2008) recommends using a 0.70 threshold to filter out cloudy scenes, so 0.75 is a proper threshold to remove both cloudy scenes and heavy aerosol load situations.

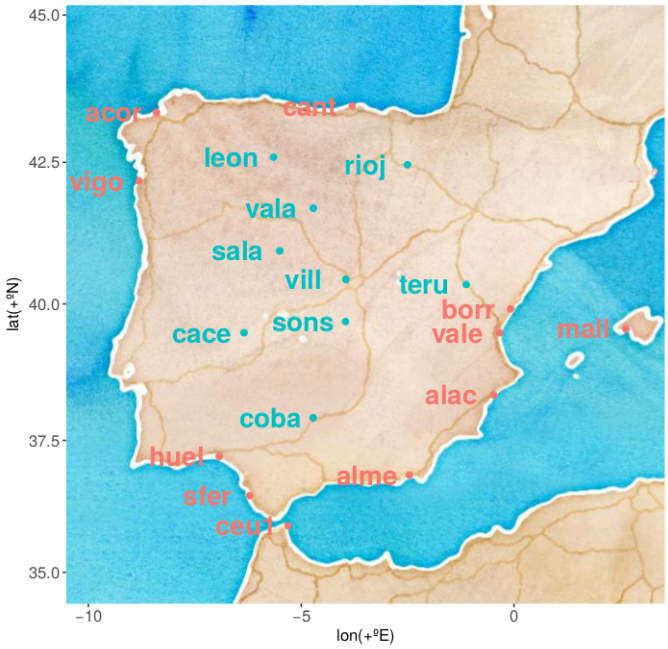

Figure 1: Location of the twenty stations selected. Coastal station are written in red and inland stations in blue.

Station	Acronym	Latitude (°N)	Longitude (°E)	Altitude (m)
A Coruña	acor	43.36	-8.40	12
Alicante	alac	38.34	-0.48	10
Almería	alme	36.85	-2.46	77
Burriana	borr	39.91	-0.08	22
Cáceres	cace	39.48	-6.34	384
Ceuta	ceu1	35.89	-5.31	53
Córdoba	coba	37.92	-4.72	162
Huelva	huel	37.20	-6.92	29
León	leon	42.59	-5.65	915
Logroño	rioj	42.46	-2.50	452
Mallorca	mall	39.55	2.63	62
Salamanca	sala	40.95	-5.50	800
San Fernando	sfer	36.46	-6.21	4
Santander	cant	43.47	-3.80	48
Sonseca	sons	39.68	-3.96	755
Teruel	teru	40.35	-1.12	956
Valencia	vale	39.48	-0.34	28
Valladolid	vala	41.70	-4.71	766
Vigo	vigo	42.18	-8.81	33
Villafranca	vill	40.44	-3.95	596

Table 1: Location of GPS stations considered

3. Water vapor radiative effect

SW irradiances at surface were simulated by means of Santa Barbara's DISORT Radiative Transfer model (SBDART), under cloud and aerosol free conditions using a radiative transfer solver with 4 streams. Detailed information about this radiative transfer code can be found in Ricchiazzi et al. (1998). This model was fed with hourly IWV data, recorded during cloud-free days. Additionally, total column ozone (daily means from ERA-Interim Reanalysis) and surface albedo (monthly means from ERA-Interim Reanalysis) were used as input in the simulations. For more information on ERA-Interim Reanalysis, refer to Dee et al. (2011). The spectral region considered ranges from 0.2 μm to 4.0 μm. The wavelength step chosen was 0.50%, as a compromise between computational economy and precision. This becomes steps ranging from 0.001 μm up to 0.02 μm. The atmosphere models (McClatchey et al., 1972) used were SBDART's mid-latitude summer from March to August (both included) and mid-latitude winter, for the rest of the year. The water vapor profile and ozone profile are re-scaled to the total IWV and total column ozone that the model is fed with. Thermal radiation is not considered in these computations, since it is negligible in the wavelength range considered. The model was run twice for each hourly GPS measurement: once with all data mentioned above and other with the same data except for water vapor, which is set to 0 cm. This allows to obtain the WVRE as the difference between the net (downwards minus upwards) irradiance at surface simulated under an atmosphere with water vapor and the net irradiance assuming no water vapor.

$$\mathrm{WVRE} = \left(\mathrm{SW}^{\downarrow}_{\mathrm{IWV}} - \mathrm{SW}^{\uparrow}_{\mathrm{IWV}}\right) - \left(\mathrm{SW}^{\downarrow}_{\mathrm{noIWV}} - \mathrm{SW}^{\uparrow}_{\mathrm{noIWV}}\right) \tag{5}$$

At surface, this equation can be written as $\mathrm{WVRE} = (1-\alpha)\left(\mathrm{SW}^{\downarrow}_{\mathrm{IWV}} - \mathrm{SW}^{\downarrow}_{\mathrm{noIWV}}\right)$. Because SW radiation comes from the sun, nighttime (SZA $> 90°$) WVRE is automatically set to zero, without running the radiative transfer model. The

heating rates can be obtained using the expression from Liou (2002)

$$\frac{\partial T}{\partial t} = \frac{g}{C_p}\frac{\Delta \mathrm{SW}}{\Delta p} \tag{6}$$

where T is the temperature, t is the time, $g = 9.81$ ms^{-2} is the gravitational acceleration, $C_p \simeq 1004$ Jkg^{-1}K^{-1} is the specific heat of dry air, SW is the net flux in the range mentioned above, and p is the pressure. In this study, the water vapor heating rate is calculated for the whole atmospheric column, which is the difference in heating rates between an atmosphere with water vapor and a dry atmosphere.

Once the WVRE is obtained, it is possible to calculate the water vapor efficiency (WVEFF) as the partial derivative of WVRE with respect to IWV,

$$\mathrm{WVEFF} = \frac{\partial \mathrm{WVRE}}{\partial \mathrm{IWV}} \tag{7}$$

if a functional form for WVRE depending on IWV is suggested. This efficiency is a relevant magnitude to analyze the sensitivity of WVRE values to IWV changes in SW radiation, reporting about the relationship between the absolute variations (in physical units) in WVRE and IWV values. Thus, this magnitude can be useful to quantify the impact of IWV increases (associated with the global warming) on net solar radiation at surface and TOA.

4. Results and discussion

4.1. Sensitivity study

In order to account for the effects that the uncertainties of the input variables may have on the WVRE computation, a sensitivity analysis have been performed. For these computations, several IWV and SZA values were used (see Figure 2). Both albedo and total column ozone were considered, with extreme values of both. In the simulations with extreme albedo values, an intermediate value of ozone (319 DU) was used, while for simulations with extreme ozone values, an intermediate value of albedo was used (0.160). Mid-latitude winter atmosphere profile was used.

The differences betweeen extreme values of albedo and ozone are shown in Figure 2. A change in albedo from its minimum to its maximum value produces a small but noticeable change in WVRE (up to around 8 Wm^{-2}). This represents less than 5% (if using the mean value as reference). However, changes in ozone values are not important, always under 0.24 Wm^{-2} (less than 1.5%).

Regarding SZA and IWV sensitivity, Figure 3 shows the relative difference (or error) associated to an increase of 0.5° of SZA (top) or 1 mm of IWV (bottom). The differences are below 3.5% for both the change in SZA and IWV. However, in most cases differences are under 1%. The absolute differences are under 3.5 Wm^{-2} for SZA errors and 6 Wm^{-2} for IWV errors.

4.2. Spatial variability

In order to study the differences between stations, some statistics have been calculated for a SZA window of $(60.0 \pm 0.5)^\circ$, shown in a box-plot in Figure 4. The SZA window reduces the variability due to SZA, which allows a clearer analysis of the spatial differences. It can be observed that all stations present similar values, although coastal stations generally have higher IWV (because of the proximity to water masses) and stronger WVRE (because of the higher IWV). The first and third quartiles of WVRE are around -86.3 and -71.0 Wm^{-2}, although some of them can reach up to -100.0 Wm^{-2} or decrease to -38.7 Wm^{-2}.

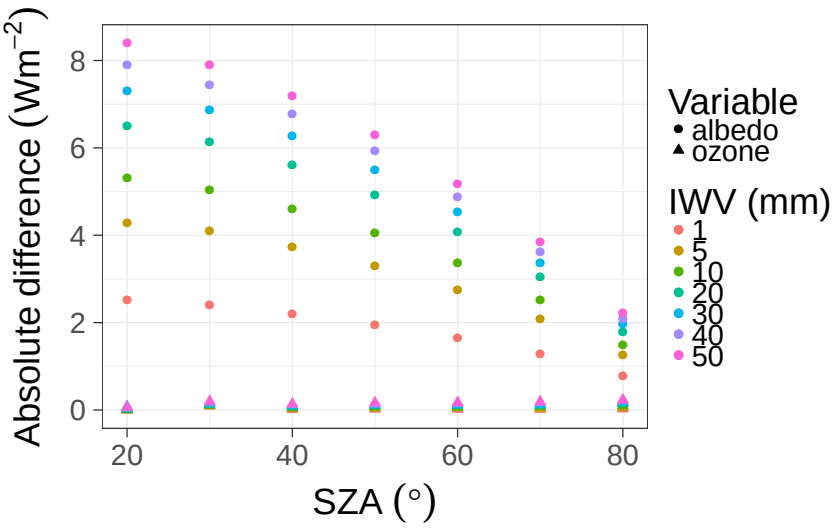

Figure 2: Sensitivity analysis of albedo and ozone. Differences between WVRE obtained using maximum and minimum values of albedo (0.146 and 0.187) and ozone (228 and 493 DU) have been calculated for several SZA and IWV values. Circles are differences of WVRE with different albedo and triangles are differences of WVRE with different total column ozone.

SD is around 10 Wm^{-2}, while the coefficient of variation (CV) is around 7%. The distributions are quite symmetric, since the median and the mean are quite similar for every station. Mateos et al. (2013b) obtained SW radiative forcing in Granada for clouds and aerosols (SZA of 60°), reporting -50 Wm^{-2} and -19 Wm^{-2}, respectively, and -69 Wm^{-2} for the combined effect of both clouds and aerosols. In the mentioned work, experimental data was used, and an empirical model was used to estimate cloud free radiation. The model was dependent on SZA and aerosol optical depth steps. This result shows that water vapor could have a greater radiative effect than clouds and aerosols in the Iberian Peninsula. On the contrary, the role of water vapor is claimed to be minor in the mentioned study. This could be related to the fact that maximum IWV considered was 25 mm, while in the present study around 20% of the data are beyond that limit. Moreover, the reference was 5 mm, instead of a totally dry atmosphere. Around a 3% of the IWV data in the present study are below

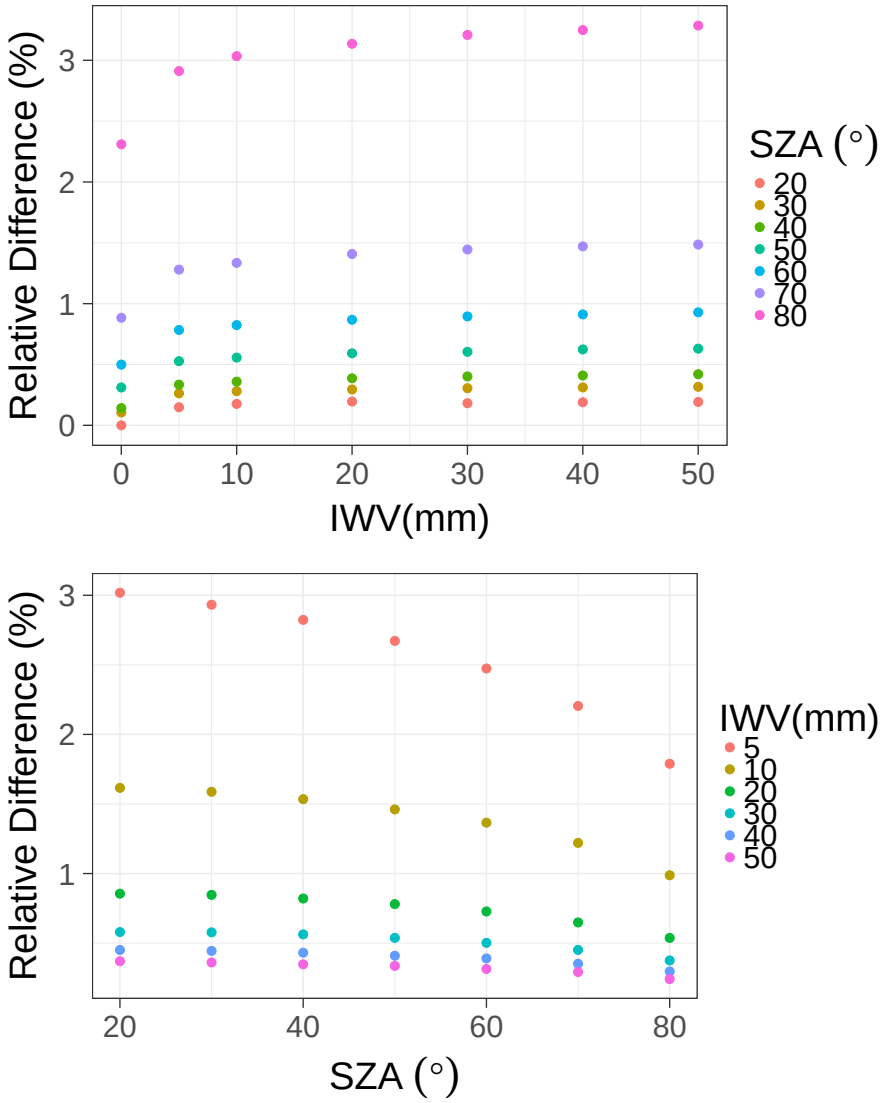

Figure 3: Sensitivity analysis of SZA and IWV. Relative differences between WVRE obtained using the value in the legend and the value plus 0.5° of SZA (top) or 1 mm (bottom) have been calculated for several SZA and IWV values.

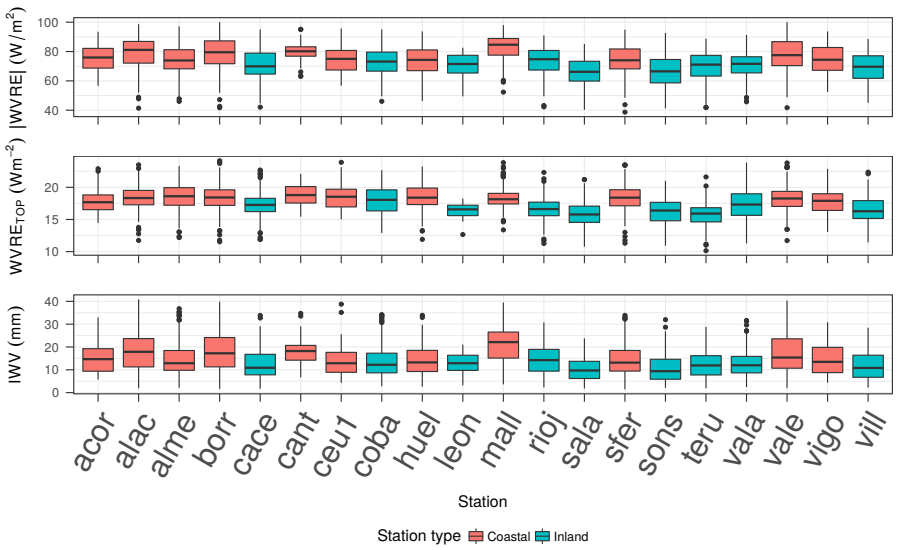

Figure 4: Boxplot of the WVRE in the ground-based stations — SZA = $(60.0 \pm 0.5)°$.

this value. Additionally, it is important to notice that while there are situations where there are no clouds, there are no situations with no water vapor at all, so the radiative effects of both clouds and water vapor are difficult to compare in a real situation.

Di Biagio et al. (2012) obtained values for WVRE in the artic region between -100 and -20 Wm^{-2}. This is somewhat below the values obtained in the present study, probably due to the fact that in the artic region, IWV is smaller $(1 - 16$ mm), and SZA values are greater as well.

Because the results show that WVRE distribution does not have a significant spatial dependence, in the following subsections all stations will be averaged together.

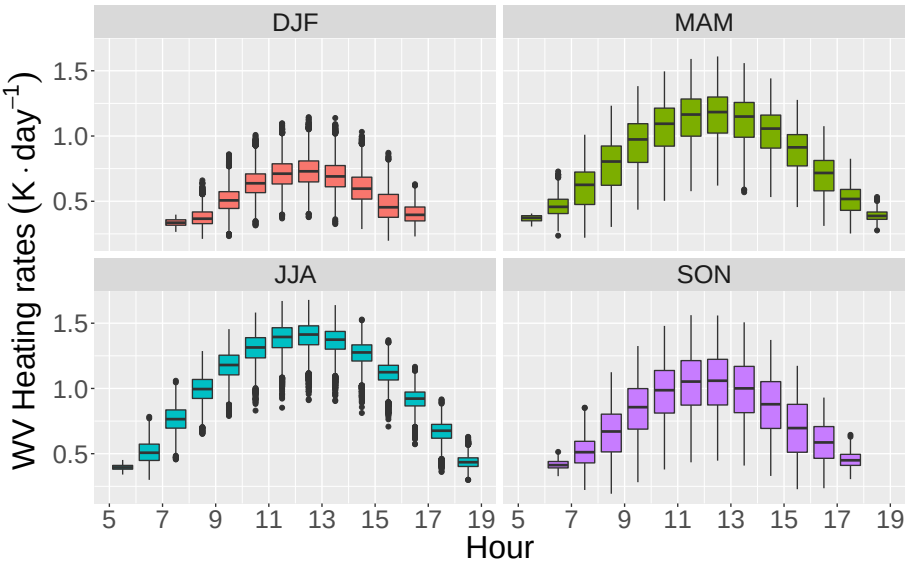

Figure 5: Boxplot of heating rates according to seasonality and hour of the day.

4.3. Water vapor effect on heating rates

Water vapor effects on heating rates, which are the difference between the heating rates (see Equation 6) with and without water vapor, show a strong dependence on the hour of the day and the season. Generally, they range between from 0.2 Kday^{-1} to 1.7 Kday^{-1}. The seasonal and hourly dependence can be observed in Figure 5. DJF values are always under 1.0 Kday^{-1}, while JJA can reach 1.5 Kday^{-1} in the central hours of the day. MAM and SON exhibit intermediate values in these hours. It must be noticed that the minimum values are in the four seasons quite similar, around 0.3 Kday^{-1}. This is a quite strong value if compared with aerosols, as shown in Valenzuela et al. (2012), where aerosol heating rates are reported to be always below 0.3 Kday^{-1}.

4.4. Empirical model for WVRE

The results of WVRE for every hour show a high degree of correlation with IWV and SZA (more concisely, with $\mu = \cos \mathrm{SZA}$), as shown in Figure 6. On the one hand, the amount of water vapor will obviously have an impact on SW

radiation at surface: the higher the IWV, the stronger the abortion effects. On the other hand, SZA has a double effect. First, optical mass increases with SZA, increasing radiative effect. Additionally, the larger the SZA is, the smaller the intensity of incoming radiation on a horizontal surface, due to the stronger absorption by other atmospheric gases and the geometric effect caused by non-verticality.

Because of the linear behavior of the log-log plots in Figure 6, the best fit appears to be the one shown in Equation 8

$$\mathrm{WVRE} = -a \cdot \mathrm{IWV}^{b} \mu^{c} \tag{8}$$

which can be linearized for a multi-linear regression in the form of Equation 9

$$\log|\mathrm{WVRE}| = \log(a) + b \log \mathrm{IWV} + c \log(\mu) \tag{9}$$

In these equations, WVRE is in Wm^{-2} and IWV in mm. Similar empirical models have been proposed for other atmospheric gases (i.e. ozone, see Madronich (2007)). The result of this multi-linear model gives a Pearson's Coefficient of $R^2 = 0.997$. The coefficients are $\log(a) = 4.144 \pm 0.001$, $b = 0.2661 \pm 0.0003$ and $c = 0.7679 \pm 0.0003$.

This model represents an empirical formula for WVRE depending on μ, the cosine of SZA, and IWV. Black, dashed lines in Figure 6 represent this fit for SZA = 30.05° and SZA = 50.05° (left) and for IWV = 25.05 mm and IWV = 40.05 mm (right), with very good agreement.

In this model, the physical meaning of the slope b is the ratio between relative changes in WVRE and relative changes of IWV. For small changes of IWV, we can derive b from Equation 8 as

$$b = \frac{\Delta\mathrm{WVRE}/\mathrm{WVRE}}{\Delta\mathrm{IWV}/\mathrm{IWV}}. \tag{10}$$

This means that a change of 1 % in IWV would cause a change of b % in WVRE, that is to say, ~ 0.27 %. The interpretation of b is similar to that of the Radiation Amplification Factor (RAF) used as a measure of sensitivity of

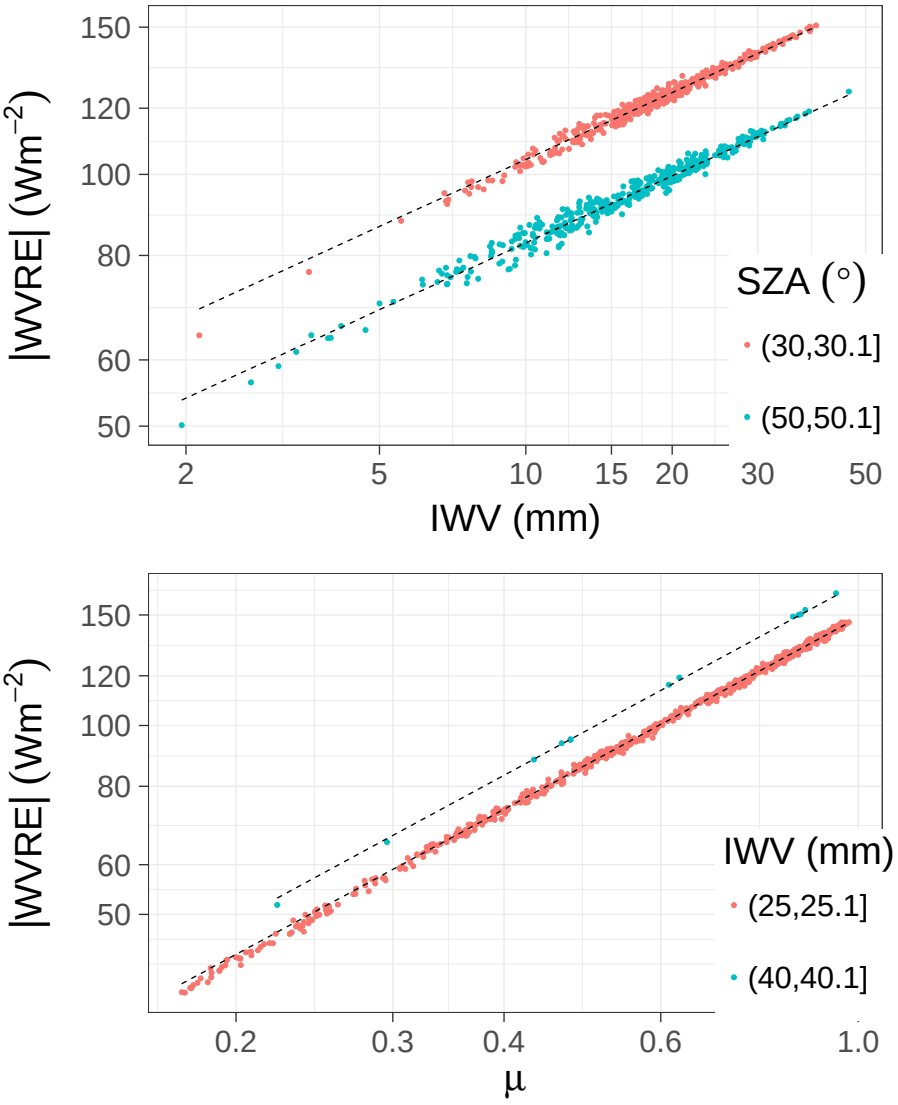

Figure 6: WVRE against IWV (up) and μ (down) in a log-log plot. The dashed, black lines show the fit. The legends show the intervals of SZA and IWV values considered.

ultraviolet solar radiation to changes in total ozone column (McKenzie et al., 1991).

Normalized WVRE ($100\% \cdot \mathrm{WVRE}/\left(\mathrm{SW}^{\downarrow}_{\mathrm{noIWV}} - \mathrm{SW}^{\uparrow}_{\mathrm{noIWV}}\right)$) is between -6.9 and -28.1%. The same approach can be followed with this variable. The multi-linear model gives good results ($R^2 = 0.9891$), with $\log(a_N) = 1.7374 \pm 0.0004$, $b_N = 0.2826 \pm 0.0001$ and $c_N = -0.3252 \pm 0.0002$.

4.5. Water vapor efficiency calculation

The empirical model obtained in the previous section can be used to obtain water vapor radiative efficiency (WVEFF) as the derivative of WVRE with respect to IWV (see Equation 7).

$$\mathrm{WVEFF} = -a \cdot \mu^c \cdot b \cdot \mathrm{IWV}^{b-1} = b\frac{\mathrm{WVRE}}{\mathrm{IWV}} \tag{11}$$

WVEFF has been calculated for some different SZA bins. The result is shown in Figure 7, where WVEFF is plotted against SZA (a) and IWV (b). It can be noticed that in all cases WVEFF decreases as SZA increases, and for a certain value of SZA, WVEFF decreases as IWV increases. Figure 7 (b) shows that WVEFF decreases as IWV increases, very sharply at small IWV, while saturating for greater IWV. For a fixed value of IWV, WVEFF decreases as SZA increases. A similar dependence of clouds radiative efficiency on SZA was observed in Mateos et al. (2014b), although the functional form was different. WVEFF dependence on SZA can be explained in the following way: vertical solar irradiance decreases with SZA, decreasing the amount of radiation available for water vapor to absorb, and therefore decreasing its efficiency. Nevertheless, there could be a second order effect, as water vapor optical mass increases with SZA, increasing the extinguishing power of water vapor, but this is not noticeable in these results. However, using the same approach for normalized WVRE as for WVRE, as shown in Figure 7 (c) and (d), we can eliminate the first effect and the second is revealed. In Figure 7 (c), it can be seen that the dependence on SZA is weaker as IWV increases, due to the saturating effect of high IWV. As an increase of SZA causes an increase in the water vapor optical mass, if IWV is already large the saturation causes small values of WVEFF.

Figure 8 shows a time series of WVEFF and IWV. The WVEFF values are typically around -8 and 0 Wm^{-2}mm, and normalized WVEFF between -2 and 0 %/mm. It can be observed that for small IWV, WVEFF is stronger. Therefore, the annual and diurnal cycle of WVEFF is related to IWV and modulated by SZA.

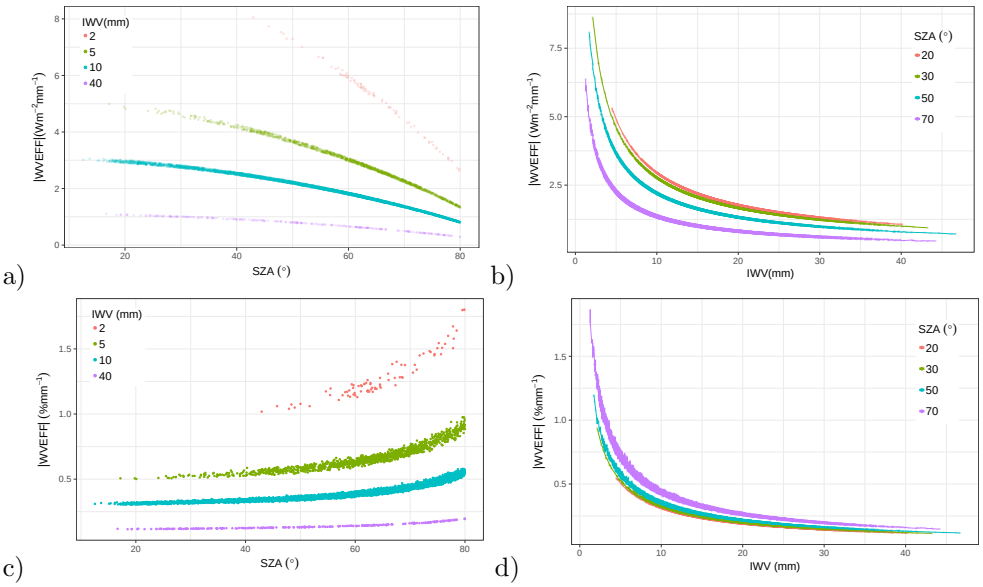

Figure 7: WVEFF (without sign) against SZA (a) for several IWV bins, and against IWV (b) for several SZA bins. (c) and (d) are similar but for normalized WVEFF (without sign).

fig:wvre

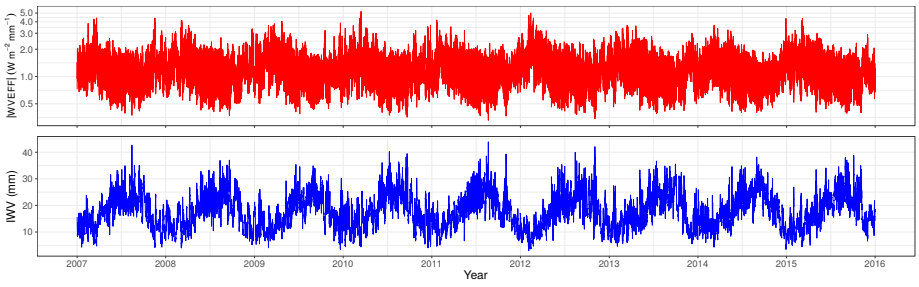

Figure 8: Time series of WVEFF (a) and IWV (b)

4.6. Effects on top of atmosphere

The WVRE and WVEFF has also been calculated at TOA ($\mathrm{WVRE_{TOP}}$ and $\mathrm{WVEFF_{TOP}}$). Figure 4 shows the boxplots of $\mathrm{WVRE_{TOP}}$ for every station. The variability is quite small, varying from 11.3 to 21.3 $\mathrm{Wm^{-2}}$. If the relative $\mathrm{WVRE_{TOP}}$ is calculated, the values are between 1.7 and 5.7%. These small values are expected, since the downwards flux is the same with and without the water vapor, and the upward fluxes are small in both cases. The small normalized values are explained taking into account that the neat flux without water vapor is quite similar at top of the atmosphere and at surface (maximum variation are around 6 %). So the denominator is similar in both cases, whil the numerator (WVRE) is smaller at TOA than at surface. The influence of albedo in $\mathrm{WVRE_{TOP}}$ is more important than at surface. The reason is that the downwards fluxes are the same with and without water vapor, so they cancel out, so the upwards fluxes (which depend on albedo) are the main contribution to $\mathrm{WVRE_{TOP}}$. The values are always positive. Therefore, a empirical expression for $\mathrm{WVRE_{TOP}}$ as a function of SZA, IWV and albedo can be found:

$$\mathrm{WVRE_{TOP}} = a_{\mathrm{TOP}} \cdot \mathrm{IWV}^{b_{TOP}} \mu^{c_{\mathrm{TOP}}} \alpha^{d_{\mathrm{TOP}}} \tag{12}$$

Correlation is $R^2 = 0.9931$, and the coefficients are $\log(a_{\mathrm{TOP}}) = 4.567 \pm 0.003$, $b_{\mathrm{TOP}} = 0.2264 \pm 0.0003$, $c_{\mathrm{TOP}} = 0.8785 \pm 0.0003$ and $d_{\mathrm{TOP}} = 0.933 \pm 0.002$. The linear relationship and the effect of albedo can be noticed in Figure 9.

Using the same methodology, $\mathrm{WVEFF_{TOP}} = b_{\mathrm{top}} \frac{\mathrm{WVRE_{TOP}}}{\mathrm{IWV}}$. The dependence of $\mathrm{WVEFF_{TOP}}$ on SZA and IWV is quite similar to the observed for WVEFF in Figure 7, but the scale is different: $\mathrm{WVEFF_{TOP}}$ ranges from 0 to 1.6 $\mathrm{Wm^{-2}mm^{-1}}$ and in relative terms, from 0 to 0.3 $\%\mathrm{mm^{-1}}$. The effect is weaker at TOA than at surface, both in absolute and relative terms.

5. Conclusions

In this work, WVRE under cloud-free conditions has been obtained from radiative transfer model SBDART in the context of the Iberian Peninsula. Val-

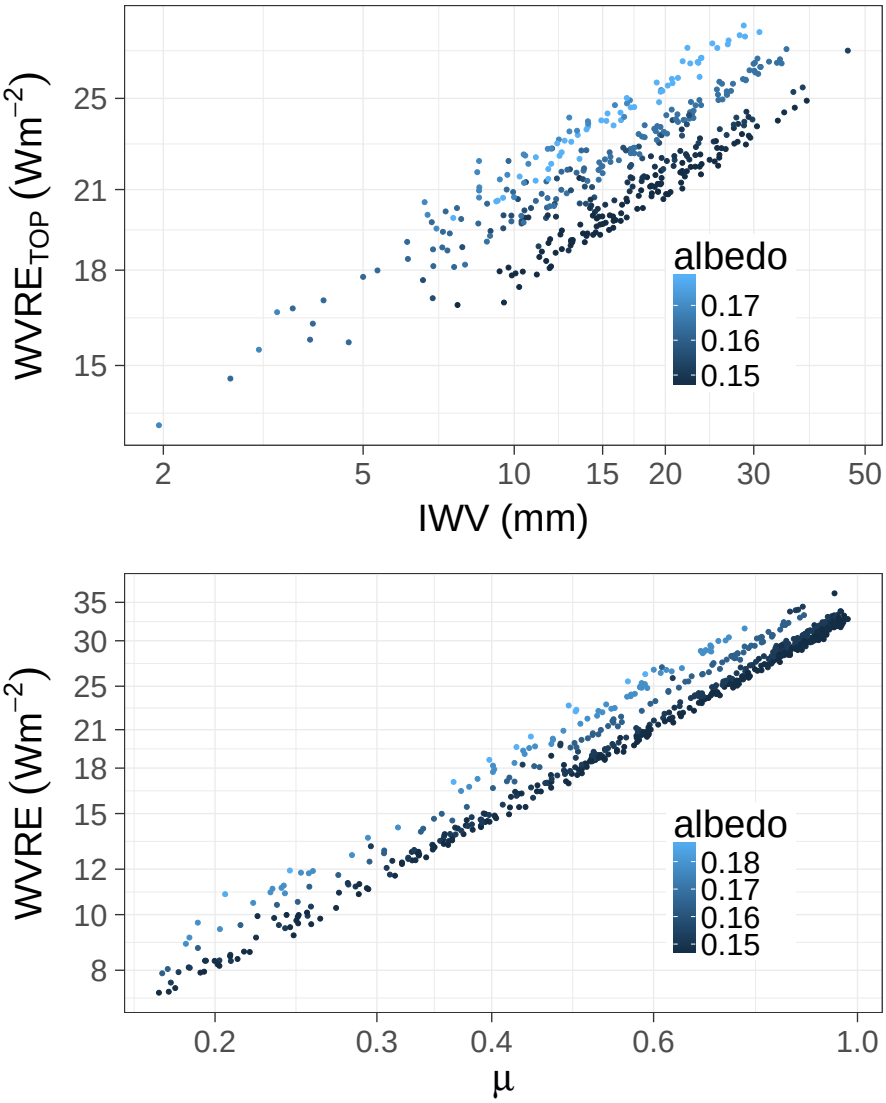

Figure 9: WVRE against IWV (up) and μ (down) in a log-log plot. The legends show the intervals of SZA and IWV values considered.

ues, for $59.5° < \mathrm{SZA} < 60.5°$, are between -100.0 (for IWV = 39.8 mm) and -38.7 Wm^{-2} (for IWV = 1.4 mm) , which points out the high radiative effect related to the water vapor. All stations considered showed similar values of WVRE, although slight differences could be noticed between coastal and inland stations. Heating rates were also calculated, being always between 0.2 and 1.5 Kday^{-1}. Moreover, a power relation between WVRE and μ and IWV has been proposed, with a high degree of correlation. The same approach has been followed for normalized WVRE, with similar results.

Then, from the proposed empirical relation, WVEFF has been found, by applying the first derivative of WVRE with respect to IWV. WVEFF showed a decrease with increasing IWV, sharply at small IWV and saturating for greater IWV. This happens because the more water vapor in the atmosphere, the more radiation is absorbed by it, and thus less radiation is available for the lower layers of water vapor to absorb. This results in a decrease of efficiency.

With increasing SZA, WVEFF decreases, in a relatively steady manner. When SZA increases, the incoming radiation is smaller, and thus efficiency is diminished. WVEFF values are around -8 and 0 $\mathrm{Wm}^{-2}\mathrm{mm}^{-1}$ (-1.8 and 0 $\%/\mathrm{mm}^{-1}$).

Following the same approach as before, relative WVEFF was calculated from normalized WVRE. It showed a similar relation with IWV, but an opposed relation with SZA: increasing SZA resulted in higher relative WVEFF. When SZA increases, water vapor's optical mass increases, increasing its efficiency.

The effect of water vapor was also analyzed at TOA, where it is positive and weaker than in the surface. For $59.5° < \mathrm{SZA} < 60.5°$, it goes from 11.3 (for IWV = 1.44 mm) to 20.3 Wm^{-2} (for IWV = 39.8 mm). The influence of albedo is higher and was included in the empirical formula. The behaviour of $\mathrm{WVEFF}_{\mathrm{TOP}}$ is similar to WVEFF, but positive and much weaker, ranging between 0 and 1.6 $\mathrm{Wm}^{-2}\mathrm{mm}^{-1}$ (0 and 0.3 $\%/\mathrm{mm}^{-1}$).

Acknowledgments

This work was supported by the Spanish Ministry of Economy and Competitiveness through project CGL2014-56255-C2. Support from the Junta de Extremadura (Research Group Grants GR15137) is gratefully acknowledged. Work at Universidad de Valladolid is supported by project CMT2015-66742-R. Work at Universidad de Granada was supported by the Andalusia Regional Government (project P12-RNM-2409) and the Spanish Ministry of Economy and Competitiveness and FEDER funds under the projects CGL2016-81092-R and "Juan de la Cierva-Formación" program (FJCI-2014-22052). Some free software was used in this work: GNU Parallel (Tange, 2011), for parallel processing of SBDART's calls; R (R Core Team, 2017), for data analysis, as well as some of its packages, such as ggplot2 (Wickham, 2009), ggmap (Kahle & Wickham, 2013), xtable (Dahl, 2016), reshape (Wickham, 2007), plyr (Wickham, 2011), chron (James & Hornik, 2014) and memisc (Elff, 2017).

References

Antón, M., Cazorla, A., Mateos, D., Costa, M. J., Olmo, F. J., & Alados-Arboledas, L. (2016). Sensitivity of UV Erythemal Radiation to Total Ozone Changes under Different Sky Conditions: Results for Granada, Spain. *Photochemistry and Photobiology*, *92*, 215–219. doi:10.1111/php.12539.

Antón, M., & Mateos, D. (2013). Shortwave radiative forcing due to long-term changes of total ozone column over the Iberian Peninsula. *Atmospheric Environment*, *81*, 532–537. doi:10.1016/j.atmosenv.2013.09.047.

Bennouna, Y. S., Torres, B., Cachorro, V. E., Ortiz de Galisteo, J. P., & Toledano, C. (2013). The evaluation of the integrated water vapour annual cycle over the Iberian Peninsula from EOS-MODIS against different ground-based techniques. *Quarterly Journal of the Royal Meteorological Society*, *139*, 1935–1956. doi:10.1002/qj.2080.

Bevis, M., Businger, S., Herring, T. A., Rocken, C., Anthes, R. A., & Ware, R. H. (1992). GPS Meteorology: Remote Sensing of Atmospheric Water Vapor Using the Global Positioning System. *Journal of Geophysical Research*, *97*, 15787–15801. URL: http://doi.wiley.com/10.1029/92JD01517. doi:10.1029/92JD01517.

Colman, R. (2003). A comparison of climate feedbacks in general circulation models. *Climate Dynamics*, *20*, 865–873. URL: http://link.springer.com/article/10.1007/s00382-003-0310-z. doi:10.1007/s00382-003-0310-z.

Dahl, D. B. (2016). *xtable: Export Tables to LaTeX or HTML*. URL: https://CRAN.R-project.org/package=xtable r package version 1.8-2.

Dee, D. P., Uppala, S. M., Simmons, A. J., Berrisford, P., Poli, P., Kobayashi, S., Andrae, U., Balmaseda, M. A., Balsamo, G., Bauer, P., Bechtold, P., Beljaars, A. C. M., van de Berg, L., Bidlot, J., Bormann, N., Delsol, C., Dragani, R., Fuentes, M., Geer, A. J., Haimberger, L., Healy, S. B., Hersbach, H., Hólm, E. V., Isaksen, L., Kållberg, P., Köhler, M., Matricardi, M., McNally, A. P., Monge-Sanz, B. M., Morcrette, J.-J., Park, B.-K., Peubey, C., de Rosnay, P., Tavolato, C., Thépaut, J.-N., & Vitart, F. (2011). The ERA-Interim reanalysis: configuration and performance of the data assimilation system. *Quarterly Journal of the Royal Meteorological Society*, *137*, 553–597. doi:10.1002/qj.828.

Denman, K. L., & Brasseur, G. (2007). Couplings Between Changes in the Climate System and Biogeochemistry. *Climate Change 2007: The Physical Science Basis. Contribution of Working Group I to the Fourth Assessment Report of the Intergovernmental Panel on Climate Change*, . URL: http://www.ipcc.ch/pdf/assessment-report/ar4/wg1/ar4-wg1-chapter7.pdf.

Di Biagio, C., di Sarra, A., Eriksen, P., Ascanius, S. E., Muscari, G., & Holben, B. (2012). Effect of surface albedo, water vapour, and atmospheric

aerosols on the cloud-free shortwave radiative budget in the Arctic. *Climate Dynamics*, *39*, 953–969. URL: http://link.springer.com/10.1007/s00382-011-1280-1. doi:10.1007/s00382-011-1280-1.

Elff, M. (2017). *memisc: Tools for Management of Survey Data and the Presentation of Analysis Results*. URL: https://CRAN.R-project.org/package=memisc r package version 0.99.13.

Forster, P. M. D. F., & Shine, K. P. (2002). Assessing the climate impact of trends in stratospheric water vapor. *Geophysical Research Letters*, *29*, 10–1–10–4. URL: http://doi.wiley.com/10.1029/2001GL013909. doi:10.1029/2001GL013909.

James, D., & Hornik, K. (2014). *chron: Chronological Objects which Can Handle Dates and Times*. URL: http://CRAN.R-project.org/package=chron r package version 2.3-45. S original by David James, R port by Kurt Hornik.

Kahle, D., & Wickham, H. (2013). ggmap: Spatial visualization with ggplot2. *The R Journal*, *5*, 144–161. URL: http://journal.r-project.org/archive/2013-1/kahle-wickham.pdf.

Liou, K. (2002). *An Introduction to Atmospheric Radiation*. Elsevier: Elsevier, New York, USA.

Madronich, S. (2007). Analytic Formula for the Clear-sky UV Index. *Photochemistry and Photobiology*, *83*, 1537–1538. URL: http://doi.wiley.com/10.1111/j.1751-1097.2007.00200.x. doi:10.1111/j.1751-1097.2007.00200.x.

Mateos, D., Antón, M., Sanchez-Lorenzo, A., Calbó, J., & Wild, M. (2013a). Long-term changes in the radiative effects of aerosols and clouds in a mid-latitude region (1985–2010). *Global and Planetary Change*, *111*, 288–295. URL: http://linkinghub.elsevier.com/retrieve/pii/S0921818113002233. doi:10.1016/j.gloplacha.2013.10.004.

Mateos, D., Antón, M., Toledano, C., Cachorro, V. E., Alados-Arboledas, L., Sorribas, M., Costa, M. J., & Baldasano, J. M. (2014a). Aerosol radiative effects in the ultraviolet, visible, and near-infrared spectral ranges using long-term aerosol data series over the Iberian Peninsula. *Atmospheric Chemistry and Physics*, *14*, 13497–13514. URL: http://www.atmos-chem-phys.net/14/13497/2014/. doi:10.5194/acp-14-13497-2014.

Mateos, D., Antón, M., Valenzuela, A., Cazorla, A., Olmo, F., & Alados-Arboledas, L. (2014b). Efficiency of clouds on shortwave radiation using experimental data. *Applied Energy*, *113*, 1216–1219. URL: http://linkinghub.elsevier.com/retrieve/pii/S0306261913007046. doi:10.1016/j.apenergy.2013.08.060.

Mateos, D., Antón, M., Valenzuela, A., Cazorla, A., Olmo, F. J., & Alados-Arboledas, L. (2013b). Short-wave radiative forcing at the surface for cloudy systems at a midlatitude site. *Tellus B: Chemical and Physical Meteorology*, *65*, 21069. URL: https://www.tandfonline.com/doi/full/10.3402/tellusb.v65i0.21069. doi:10.3402/tellusb.v65i0.21069.

McClatchey, R. A., Fenn, R. W., Selby, J. E. A., Volz, F. E., & Garing, J. S. (1972). *Optical Properties of the Atmosphere (Third Edition)*. URL: http://oai.dtic.mil/oai/oai?verb=getRecord{&}metadataPrefix=html{&}identifier=AD0753075.

McKenzie, R. L., Matthews, W. A., & Johnston, P. V. (1991). The relationship between erythemal UV and ozone, derived from spectral irradiance measurements. *Geophysical Research Letters*, *18*, 2269–2272. doi:10.1029/91GL02786.

Myhre, G., Shindell, D., Bréon, F.-M., Collins, W., Fuglestvedt, J., Huang, J., Koch, D., Lamarque, J.-F., Lee, D., Mendoza, B., Nakajima, T., Robock, A., Stephens, G., Takemura, T., & Zhang, H. (2013). Anthropogenic and Natural Radiative Forcing. In *Climate Change 2013: The Physical Science*

Basis. Contribution of Working Group I to the Fifth Assessment Report of the Intergovernmental Panel on Climate Change (pp. 659–740).

R Core Team (2017). *R: A Language and Environment for Statistical Computing*. R Foundation for Statistical Computing Vienna, Austria. URL: https://www.R-project.org/.

Ricchiazzi, P., Yang, S., Gautier, C., & Sowle, D. (1998). SBDART: A Research and Teaching Software Tool for Plane-Parallel Radiative Transfer in the Earth's Atmosphere. *Bulletin of the American Meteorological Society*, *79*, 2101–2114. URL: http://journals.ametsoc.org/doi/abs/10.1175/1520-0477{%}281998{%}29079{%}3C2101{%}3ASARATS{%}3E2.0.CO{%}3B2. doi:10.1175/1520-0477(1998)079<2101:SARATS>2.0.CO;2.

Román, R., Antón, M., Cachorro, V., Loyola, D., Ortiz de Galisteo, J., de Frutos, A., & Romero-Campos, P. (2015). Comparison of total water vapor column from GOME-2 on MetOp-A against ground-based GPS measurements at the Iberian Peninsula. *Science of The Total Environment*, *533*, 317–328. URL: http://linkinghub.elsevier.com/retrieve/pii/S0048969715303260. doi:10.1016/j.scitotenv.2015.06.124.

Román, R., Bilbao, J., & de Miguel, A. (2014). Uncertainty and variability in satellite-based water vapor column, aerosol optical depth and Angström exponent, and its effect on radiative transfer simulations in the Iberian Peninsula. *Atmospheric Environment*, *89*, 556–569. URL: http://linkinghub.elsevier.com/retrieve/pii/S135223101400123X. doi:10.1016/j.atmosenv.2014.02.027.

Santer, B. D., Mears, C., Wentz, F. J., Taylor, K. E., Gleckler, P. J., Wigley, T. M. L., Barnett, T. P., Boyle, J. S., Bruggemann, W., Gillett, N. P., Klein, S. A., Meehl, G. A., Nozawa, T., Pierce, D. W., Stott, P. A., Washington, W. M., & Wehner, M. F. (2007). Identification of human-induced changes in atmospheric moisture content. *Proceedings of the National Academy of Sciences*, *104*, 15248–15253. URL: http://www.pubmedcentral.nih.gov/

articlerender.fcgi?artid=1986574{&}tool=pmcentrez{&}rendertype=abstracthttp://www.pnas.org/cgi/doi/10.1073/pnas.0702872104. doi:10.1073/pnas.0702872104.

Smith, C. A., Haigh, J. D., & Toumi, R. (2001). Radiative forcing due to trends in stratospheric water vapour. *Geophysical Research Letters*, *28*, 179–182. URL: http://doi.wiley.com/10.1029/2000GL011846. doi:10.1029/2000GL011846.

Soden, B. J., Wetherald, R. T., Stenchikov, G. L., & Robock, A. (2002). Global Cooling After the Eruption of Mount Pinatubo: A Test of Climate Feedback by Water Vapor. *Science*, *296*, 727–730. URL: http://www.sciencemag.org/cgi/doi/10.1126/science.296.5568.727. doi:10.1126/science.296.5568.727.

Solomon, S., Rosenlof, K., Portmann, R., Daniel, J., Davis, S., Sanford, T., & Plattner, G.-K. (2010). Contributions of Stratospheric Water Vapor to Decadal Changes in the Rate of Global Warming. *Science*, *327*, 1219–1223. URL: http://www.sciencemag.org/cgi/content/abstract/327/5970/1219http://www.sciencemag.org/cgi/doi/10.1126/science.1182488. doi:10.1126/science.1182488.

Tange, O. (2011). GNU Parallel: The Command-Line Power Tool. *;login: The USENIX magazine*, *36*, 42–47. URL: https://www.usenix.org/system/files/login/articles/105438-Tange.pdf.

Valenzuela, A., Olmo, F. J., Lyamani, H., Antón, M., Quirantes, A., & Alados-Arboledas, L. (2012). Aerosol radiative forcing during African desert dust events (2005–2010) over Southeastern Spain. *Atmospheric Chemistry and Physics*, *12*, 10331–10351. URL: http://www.atmos-chem-phys.net/12/10331/2012/. doi:10.5194/acp-12-10331-2012.

Vaquero-Martínez, J., Antón, M., Ortiz de Galisteo, J. P., Cachorro, V. E., Costa, M. J., Román, R., & Bennouna, Y. S. (2017a). Validation of MODIS

integrated water vapor product against reference GPS data at the Iberian Peninsula. *International Journal of Applied Earth Observation and Geoinformation*, *63*, 214–221. URL: http://linkinghub.elsevier.com/retrieve/pii/S0048969716327176. doi:10.1016/j.jag.2017.07.008.

Vaquero-Martínez, J., Antón, M., Ortiz de Galisteo, J. P., Cachorro, V. E., Wang, H., González Abad, G., Román, R., & Costa, M. J. (2017b). Validation of integrated water vapor from OMI satellite instrument against reference GPS data at the Iberian Peninsula. *Science of The Total Environment*, *580*, 857–864. URL: http://linkinghub.elsevier.com/retrieve/pii/S0048969716327176. doi:10.1016/j.scitotenv.2016.12.032.

Wickham, H. (2007). Reshaping data with the reshape package. *Journal of Statistical Software*, *21*, 1–20. URL: http://www.jstatsoft.org/v21/i12/.

Wickham, H. (2009). *ggplot2: Elegant Graphics for Data Analysis*. Springer-Verlag New York. URL: http://ggplot2.org.

Wickham, H. (2011). The split-apply-combine strategy for data analysis. *Journal of Statistical Software*, *40*, 1–29. URL: http://www.jstatsoft.org/v40/i01/.

World Meteorological Organization (2008). *Guide to meteorological instruments and methods of observation* volume I. Geneva: WMO. OCLC: 785715260.

Zhong, W., & Haigh, J. D. (2003). Shortwave radiative forcing by stratospheric water vapor. *Geophysical Research Letters*, *30*, 1113. URL: http://doi.wiley.com/10.1029/2002GL016042. doi:10.1029/2002GL016042.